Energies **2012**, *5*, 4758-4778; doi:10.3390/en5114758

OPEN ACCESS

energies

ISSN 1996-1073

www.mdpi.com/journal/energies

Article

Proportional-Resonant Control of Doubly-Fed Induction Generator Wind Turbines for Low-Voltage Ride-Through Enhancement

Yan Yan [1,*], Meng Wang [2], Zhan-Feng Song [1] and Chang-Liang Xia [1,3]

[1] School of Electrical Engineering and Automation, Tianjin University, Tianjin 300072, China; E-Mails: zfsong@tju.edu.cn (Z.-F.S.); motor@tju.edu.cn (C.-L.X.)

[2] College of Physics & Electronic Engineering, Henan Normal University, Xinxiang 453007, China; E-Mail: wangmeng@htu.cn

[3] School of Electrical Engineering & Automation, Tianjin Polytechnic University, Tianjin 300160, China

* Author to whom correspondence should be addressed; E-Mail: yanyan@tju.edu.cn; Tel./Fax: +86-22-27402325.

Received: 6 September 2012; in revised form: 5 November 2012 / Accepted: 5 November 2012 / Published: 19 November 2012

Abstract: A novel control strategy is proposed in this paper for the rotor side converter (RSC) of doubly-fed induction generator (DFIG)-based wind power generation systems. It is supposed to enhance the low-voltage ride-through (LVRT) capability of DFIGs during great-level grid voltage dips. The strategy consists of a proportional-resonant (PR) controller and auxiliary PR controllers. The auxiliary controllers compensate the output voltage of the RSC in case of grid faults, thus limiting the rotor inrush current of DFIG and meeting the requirements of LVRT. Sequential-component decompositions of current are not required in the control system to improve the response of system. Since the resonant compensator is a double-side integrator, the auxiliary controllers can be simplified through coordinate transformation. The feasibility of the control strategy is validated by simulation on a 1.5 MW wind-turbine driven DFIG system. The impact of the RSC converter voltage rating on the LVRT capability of DFIG is investigated. Meanwhile, the influence of angular frequency detection and control parameters are also discussed. Compared with traditional vector control schemes based on PI current controllers, the presented control strategy effectively suppress rotor current and reduce oscillations of DFIG power and torque under grid faults.

Keywords: doubly-fed induction generator (DFIG); grid faults; low-voltage ride-through (LVRT); proportional-resonant (PR) controller

Nomenclature

U_s, U_r	Stator and rotor voltage vectors.
I_s, I_r	Stator and rotor current vectors.
ψ_s, ψ_r	Stator and rotor flux linkage vectors.
ω_s, ω_r	Stator and rotor angular frequencies.
L_s, L_r	Stator and rotor self inductances.
L_{ls}, L_{lr}	Stator and rotor leakage inductances.
L_m	Mutual inductance.
R_s, R_r	Stator and rotor resistances
Subscripts	
α, β	Stationary α–β axis.
s, r	Stator, rotor.
$+$, DC, $-$	Positive, DC and negative components.
0, 1, 2	Positive, DC and negative components in rotor αr βr reference frame.
Superscripts	
r	Rotor α^r β^r reference frames.
*	Reference value for controller.

1. Introduction

The doubly-fed induction generator (DFIG) has been widely used in the variable-speed constant-frequency (VSCF) wind energy conversion systems as a result of its low converter capacity and independent control of active/reactive powers [1–5]. The stator of the DFIG is directly connected to the grid, while the rotor is linked to the grid by a back-to-back converter [6,7]. A rotor side converter (RSC) is applied to control generator speed and reactive power, and a grid side converter (GSC) is adopted to control dc-link voltage. With the stator directly connected to the grid, the DFIG is very sensitive to grid faults, especially to voltage dips [8]. An abrupt drop of grid voltage causes stator voltage sag and stator current oscillations, stator active/reactive power and electromagnetic torque. Furthermore, oscillation of the stator current leads to rotor current pulsation because of the strong coupling between them, thus affecting the performance of the DFIG. When the voltage dips reach a certain level, induction wind generators are usually disconnected to protect the rotor side converter [9–11]. Large scale disconnections will further weaken the grid and cause a considerable impact on the stable grid operation. Therefore, many countries are revising their grid codes in order to keep wind turbines connected to the grid and provide reactive power compensation to the grid in the case of voltage dips [12]. Considerable research has been done on dynamic behavior and ride-through capability of DFIG-based wind turbines under grid faults. A common solution is to supply a short circuit to the rotor

windings with the crowbar, and then to disconnect the turbine from the grid to achieve the LVRT operation of wind turbines [13–15], which is easy to control and implement. For symmetrical voltage dips, the crowbar circuit only needs to be enabled at the moments of grid voltage fall and recovery to suppress rotor over-current. However, the crowbar circuit needs to be enabled throughout the whole dip due to a sustained rotor over-current caused by asymmetric voltage dips [16]. When the crowbar circuit is enabled, DFIG becomes a regular induction machine. In this case, instead of providing reactive power support to the grid, the generator absorbs large amounts of reactive power from the grid, which is not conducive to the grid recovery. To limit the rotor inrush current and enhance low voltage ride through the ability of the DFIG, appropriate control strategies for the rotor-side converter have been applied. Research on grid faults in the literature is usually classified into two categories. One is aiming at steady analysis of DFIGs during voltage unbalance [17–20]. In order to minimize the pulsation of torque and reactive power, measured torque and reactive power pulsation are used as the input of the controller to directly generate a rotor compensating voltage [17]. In [18] and [19], analysis and control of a DFIG-based wind generation system operating under unbalanced grid conditions are presented and a rotor current control strategy is used to control the rotor positive and negative sequence currents based on positive and negative reference frames. To eliminate the delay caused by positive and negative sequence decomposition of rotor current, dual current controllers are simplified by adding a resonant controller to the traditional PI controller [20]. On the other hand, various studies have been done on transient analysis in the case of voltage dips [21–23]. A new method is presented in [21], which is to generate the rotor current containing components opposite to the dc and negative sequence components in the stator flux linkage produced by grid voltage dips by controlling the rotor-side converter. To obtain the dc and negative sequence components of stator flux, a filter is usually applied. However, the response speed and stability of the control system are affected by the delay and errors caused by the filter [22]. Meanwhile, the active/reactive powers of the DFIG are no longer controlled in the case of grid faults. As referred in [23], the current coupling term affects the transient response of DFIGs under grid faults. Improved feed-forward transient compensations are added to the conventional current regulator so as to suppress the rotor fault current and enhance the LVRT capability. Negative sequence component and dc component also need to be extracted, thus leading to high computation loads and low response speeds.

To enhance the capability of LVRT for DFIGs under great-level voltage dips, a proportional-resonant (PR) current control strategy for RSC is proposed in this paper. The advantages of PR control are as follows: firstly, it requires no multiple frame transformations and be able to compensate the specified harmonic current [24–28]. Take [28] for instance, a sixth-order PR controller can be used to eliminate negative sequence fifth- and positive sequence seventh-order current harmonics induced by the lower-order voltage harmonics in the grid. Secondly, it has no coupling term affected by temperature and circuit parameters. Therefore, transient errors in the current coupling term reported in the literature [23] are avoided. In this paper, the control strategy for RSC consists of a main PR controller and auxiliary PR controllers. In the case of stator voltage dips caused by grid faults, the auxiliary controllers compensate the RSC output voltage to limit rotor fault currents without extracting dc and negative sequence components of the stator flux. Thus, it has rapid dynamic response.

This paper is organized as follows: Section 2 describes the behavior of a DFIG system under the conditions of symmetric and asymmetric grid fault. In Section 3, the DFIG control system is designed,

and the structure of auxiliary controllers is simplified. Section 4 discusses the simulation results on a 1.5-MW DFIG system, analyzes the effect of the RSC voltage ratings on the LVRT capability of DFIG system and presents the influence of angular frequency detection and control parameters on LVRT feasibility of DFIG. Section 5 draws the conclusions.

2. DFIG System Behavior during Grid Fault

As is shown in Figure 1, the generalized equivalent circuit of a DFIG is expressed in an arbitrary reference frame rotating at rotor angular speed of ω_r. According to Figure 1, the voltages and flux linkage of stator and rotor are given respectively by:

$$\begin{cases} \boldsymbol{U}^r_{s\alpha\beta} = R_s \boldsymbol{I}^r_{s\alpha\beta} + \dfrac{d}{dt}\boldsymbol{\psi}^r_{s\alpha\beta} + j\omega_r \boldsymbol{\psi}^r_{s\alpha\beta} \\ \boldsymbol{U}^r_{r\alpha\beta} = R_r \boldsymbol{I}^r_{r\alpha\beta} + \dfrac{d}{dt}\boldsymbol{\psi}^r_{r\alpha\beta} \end{cases} \tag{1}$$

$$\begin{cases} \boldsymbol{\psi}^r_{s\alpha\beta} = L_s \boldsymbol{I}^r_{s\alpha\beta} + L_m \boldsymbol{I}^r_{r\alpha\beta} \\ \boldsymbol{\psi}^r_{r\alpha\beta} = L_m \boldsymbol{I}^r_{s\alpha\beta} + L_r \boldsymbol{I}^r_{r\alpha\beta} \end{cases} \tag{2}$$

where R_s and R_r are stator and rotor resistance, $L_s = L_{ls} + L_m$ and $L_r = L_{lr} + L_m$ are the self-inductances of stator and rotor winding, L_{ls} , L_{lr} and L_m are the stator and rotor leakage inductance and mutual inductance, respectively.

Figure 1. Equivalent circuit of a DFIG in an arbitrary reference frame rotating at a speed of ω_r.

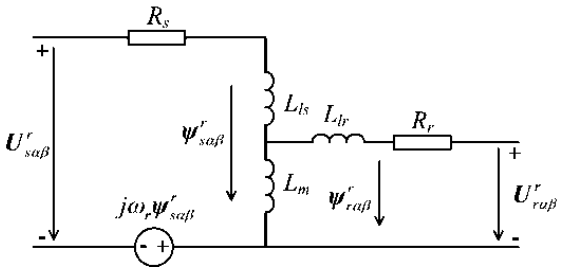

According to (2), rotor flux $\boldsymbol{\psi}^r_{r\alpha\beta}$ and stator current $\boldsymbol{I}^r_{s\alpha\beta}$ are expressed by:

$$\boldsymbol{\psi}^r_{r\alpha\beta} = \frac{L_m \boldsymbol{\psi}^r_{s\alpha\beta}}{L_s} + \sigma L_r \boldsymbol{I}^r_{r\alpha\beta} \tag{3a}$$

$$\boldsymbol{I}^r_{s\alpha\beta} = \frac{\boldsymbol{\psi}^r_{s\alpha\beta} + L_m \boldsymbol{I}^r_{r\alpha\beta}}{L_s} \tag{3b}$$

where $\sigma = 1 - L_m^2/(L_s L_r)$ is the leakage factor.

Substituting (3) into (1), the rotor voltage is calculated as:

$$\boldsymbol{U}^r_{r\alpha\beta} = R_r \boldsymbol{I}^r_{r\alpha\beta} + \sigma L_r \frac{d\boldsymbol{I}^r_{r\alpha\beta}}{dt} + \frac{L_m}{L_s}(\boldsymbol{U}^r_{s\alpha\beta} - R_s \boldsymbol{I}^r_{s\alpha\beta} - j\omega_r \boldsymbol{\psi}^r_{s\alpha\beta}) \tag{4}$$

The spatial relationship between the stator flux in the stationary reference frame ($\alpha\beta$) and that in the rotor reference frame ($\alpha^r\beta^r$) is shown in Figure 2. Suppose that ω_s is the grid angular frequency, a static dc component and a negative sequence component with the angular frequency of $-\omega_s$ appear in the stator flux linkage under grid fault conditions [21].

Figure 2. Spatial relationships between the stationary $\alpha\beta$ reference frame and the rotor $\alpha^r\beta^r$ reference frame.

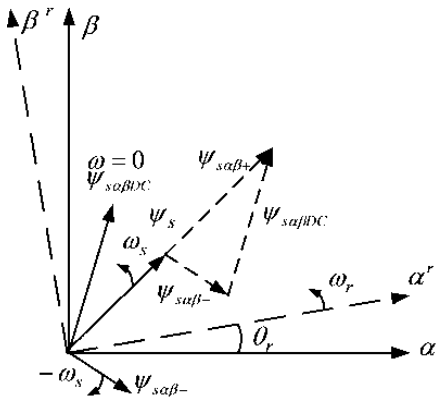

From Figure 2, the stator flux linkage in the stationary reference frame ($\alpha\beta$) is written as:

$$\boldsymbol{\psi}_{s\alpha\beta}(t) = \boldsymbol{\psi}_{s\alpha\beta+}(t) + \boldsymbol{\psi}_{s\alpha\beta DC}(t) + \boldsymbol{\psi}_{s\alpha\beta-}(t) = \left|\boldsymbol{\psi}_{s\alpha\beta+}\right| e^{j(\omega_s t+\varphi_+)} + \left|\boldsymbol{\psi}_{s\alpha\beta DC}\right| e^{-t/\tau_s} + \left|\boldsymbol{\psi}_{s\alpha\beta-}\right| e^{-j(\omega_s t+\varphi_-)} \quad (5)$$

where $\tau_s = L_s/R_s$ is attenuation time constant of dc component, φ_+ and φ_- are initial phase of positive and negative sequence component of stator flux linkage.

Positive sequence component, dc component and negative sequence component of the stator flux linkage in the stationary reference frame ($\alpha\beta$) are transformed into the rotor reference frame ($\alpha^r\beta^r$) according to Figure 2:

$$\begin{cases} \boldsymbol{\psi}^r_{s\alpha\beta+} = \boldsymbol{\psi}_{s\alpha\beta+} e^{j(\omega_s-\omega_r)t} \\ \boldsymbol{\psi}^r_{s\alpha\beta DC} = \boldsymbol{\psi}_{s\alpha\beta DC} e^{-j\omega_r t - t/\tau_s} \\ \boldsymbol{\psi}^r_{s\alpha\beta-} = \boldsymbol{\psi}_{s\alpha\beta-} e^{-j(\omega_s+\omega_r)t} \end{cases} \quad (6)$$

It is seen from Equation (6) that the fundamental current component with the angular frequency of $\omega_s - \omega_r$ and the disturbing current components with the angular frequencies of ω_r and $\omega_s + \omega_r$ will be induced by the stator flux linkage in the rotor winding.

Figure 3 depicts the stator voltage and rotor current in the three-phase stationary coordinate frame, rotor current in the rotor reference frame and its DFT analysis during stator voltage dips of 50% caused by a three-phase-to-ground grid fault. It is assumed that the grid frequency is 60 Hz and the DFIG initially operates with full load at 25% super synchronous speed. Stator voltage dips due to a three-phase grid fault as depicted in Figure 3(a). Figure 3(b) shows that a high fault current is induced in the rotor windings. Figure 3(c) gives the rotor current in the rotor reference frame. As is seen, besides the fundamental component, a harmonic component is also included in the rotor current. From the DFT analysis in Figure 3(d), it can be seen evidently that apart from the fundamental component with slip frequency of $\omega_s - \omega_r$ (15 Hz), a current component with the angular frequency of ω_r (75 Hz) also appears in the rotor winding under the influence of the dc component in the stator flux linkage

when the symmetrical voltage dips. The reason for this is that when the dc component of the stator flux rotates with the angular frequency of ω_r with respect to the rotor, a current component with the angular frequency of ω_r is induced in the rotor winding, which is a fault current of the rotor.

Figure 3. Rotor current and DFT analysis during a three-phase voltage dip. (**a**) Stator voltage; (**b**) Rotor current; (**c**) Rotor current in $\alpha^r\beta^r$ reference frame; (**d**) DFT analysis of rotor current.

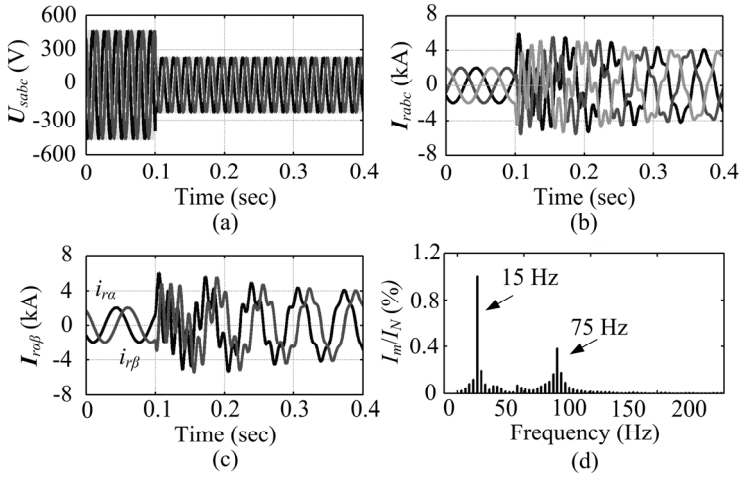

The rotor current under symmetrical voltage dip conditions is given by:

$$\boldsymbol{I}^r_{r\alpha\beta} = \boldsymbol{I}^r_{r\alpha\beta 0} + \boldsymbol{I}^r_{r\alpha\beta 1} \tag{7}$$

Substituting (7) into (4), the rotor voltage under symmetrical voltage dips is calculated as:

$$\boldsymbol{U}^r_{r\alpha\beta} = R_r\boldsymbol{I}^r_{r\alpha\beta} + \sigma L_r\left(\frac{d\boldsymbol{I}^r_{r\alpha\beta 0}}{dt} + \frac{d\boldsymbol{I}^r_{r\alpha\beta 1}}{dt}\right) + \frac{L_m}{L_s}\left(\boldsymbol{U}^r_{s\alpha\beta} - R_s\boldsymbol{I}^r_{s\alpha\beta} - j\omega_r\boldsymbol{\psi}^r_{s\alpha\beta}\right) \tag{8}$$

Figure 4 shows the stator voltage and rotor current in the three-phase stationary frame, rotor current in the rotor reference frame and its DFT analysis during stator voltage dips of 50% caused by a two-phase-to-ground fault. In the case of two-phase-to-ground dips of the stator voltage shown in Figure 4(a), it can be seen from the DFT analysis in Figure 4(d) that the rotor current in Figure 4(c) consists of current components with angular frequencies of ω_r (75 Hz) and $\omega_s + \omega_r$ (135 Hz) and a fundamental component in the rotor winding disturbed by the stator flux linkage. The reason is that when the dc and negative sequence components of stator flux rotate with the angular frequency of ω_r and $\omega_s + \omega_r$ with respect to the rotor, respectively, current components with the angular frequencies of ω_r and $\omega_s + \omega_r$ are induced in the rotor winding, which are also rotor fault currents.

The rotor current under asymmetrical voltage dips are given by:

$$\boldsymbol{I}^r_{r\alpha\beta} = \boldsymbol{I}^r_{r\alpha\beta 0} + \boldsymbol{I}^r_{r\alpha\beta 1} + \boldsymbol{I}^r_{r\alpha\beta 2} \tag{9}$$

Substituting (9) into (4), the rotor voltage under asymmetrical voltage dips is calculated as:

$$\boldsymbol{U}^r_{r\alpha\beta} = R_r\boldsymbol{I}^r_{r\alpha\beta} + \sigma L_r\left(\frac{d\boldsymbol{I}^r_{r\alpha\beta 0}}{dt} + \frac{d\boldsymbol{I}^r_{r\alpha\beta 1}}{dt} + \frac{d\boldsymbol{I}^r_{r\alpha\beta 2}}{dt}\right) + \frac{L_m}{L_s}\left(\boldsymbol{U}^r_{s\alpha\beta} - R_s\boldsymbol{I}^r_{s\alpha\beta} - j\omega_r\boldsymbol{\psi}^r_{s\alpha\beta}\right) \tag{10}$$

Figure 4. Rotor current and DFT analysis during a two-phase-to-ground voltage dip. (**a**) Stator voltage; (**b**) Rotor current; (**c**) Rotor current in $\alpha^r\beta^r$ reference frame; (**d**) DFT analysis of rotor current.

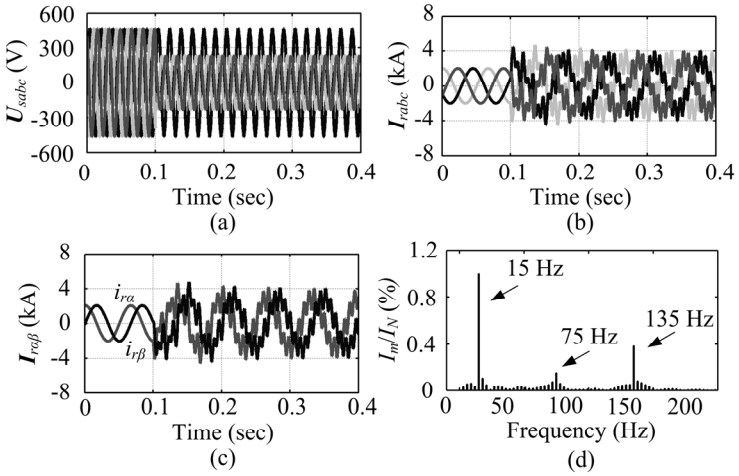

3. System Control

3.1. Proposed Control System Design

This paper presents a control scheme for the rotor side converter of a DFIG based on a PR controller. It consists of one main PR controller and two auxiliary PR controllers. The resonant frequency of the main PR controller is $\omega_s - \omega_r$ and is used to control the active/reactive powers of the DFIG. In the case of a grid fault, the auxiliary PR controllers are applied to suppress the dc and negative sequence components of the rotor current, with the resonant frequencies of ω_r and $\omega_s + \omega_r$, separately. The control scheme is implemented in the rotor reference frame without dc and negative sequence component decomposition of current. The transfer function of the main PR controller is:

$$H_m(s) = k_{p0} + \frac{k_{i0}s}{s^2 + (\omega_s - \omega_r)^2} \tag{11}$$

where k_{p0} and k_{i0} are proportion and resonant constant of main PR current controller.

The transfer functions of the two auxiliary PR controllers are:

$$\begin{cases} H_{a1}(s) = k_{p1} + \dfrac{k_{i1}s}{s^2 + \omega_r^2} \\ H_{a2}(s) = k_{p2} + \dfrac{k_{i2}s}{s^2 + (\omega_s + \omega_r)^2} \end{cases} \tag{12}$$

where k_{p1}, k_{p2}, k_{i1}, k_{i2} are proportion and resonant constants of the auxiliary controllers.

The following equation is obtained from Equation (10):

$$\sigma L_r\left(\frac{d\boldsymbol{I}^r_{r\alpha\beta}}{dt}\right) = \sigma L_r\left(\frac{d\boldsymbol{I}^r_{r\alpha\beta 0}}{dt} + \frac{d\boldsymbol{I}^r_{r\alpha\beta 1}}{dt} + \frac{d\boldsymbol{I}^r_{r\alpha\beta 2}}{dt}\right) = \boldsymbol{U}^{r*}_{r\alpha\beta} - R_r\boldsymbol{I}^r_{r\alpha\beta} - L_m / L_s(\boldsymbol{U}^r_{s\alpha\beta} - R_s\boldsymbol{I}^r_{s\alpha\beta} - j\omega_r\psi^r_{s\alpha\beta}) \tag{13}$$

where $\boldsymbol{U}^{r*}_{r\alpha\beta}$ referred to the rotor control voltage produced by the PR controller, which is designed as follows:

$$\boldsymbol{U}_{r\alpha\beta}^{r*} = \sigma L_r \boldsymbol{V}_{r\alpha\beta}^{r*} + \boldsymbol{E}_{r\alpha\beta}^{r} \tag{14}$$

where:

$$\boldsymbol{V}_{r\alpha\beta}^{r*} = \frac{d\boldsymbol{I}_{r\alpha\beta}^{r}}{dt} = \frac{d\boldsymbol{I}_{r\alpha\beta 0}^{r}}{dt} + \frac{d\boldsymbol{I}_{r\alpha\beta 1}^{r}}{dt} + \frac{d\boldsymbol{I}_{r\alpha\beta 2}^{r}}{dt} = C_{PR}(s)(\boldsymbol{I}_{r\alpha\beta}^{r*} - \boldsymbol{I}_{r\alpha\beta}^{r}) = [H_m + H_{a1} + H_{a2}](\boldsymbol{I}_{r\alpha\beta}^{r*} - \boldsymbol{I}_{r\alpha\beta}^{r}) \tag{15}$$

$$\boldsymbol{E}_{r\alpha\beta}^{r} = \sigma L_r \boldsymbol{V}_{r\alpha\beta}^{r*} + R_r \boldsymbol{I}_{r\alpha\beta}^{r} + \frac{L_m}{L_s}(\boldsymbol{U}_{s\alpha\beta}^{r} - R_s \boldsymbol{I}_{s\alpha\beta}^{r} - j\omega_r \psi_{s\alpha\beta}^{r}) \tag{16}$$

$I_{r\alpha\beta}^{r*}$ is reference value of rotor current, and $I_{r\alpha\beta}^{r}$ is actual value of rotor current.

The following equation in component form is obtained from Equations (14), (15) and (16):

$$\begin{cases} u_{r\alpha}^{r*} = \sigma L_r u_{r\alpha}^{'} + R_r i_{r\alpha}^{r} + \dfrac{L_m}{L_s} \\ \qquad (u_{s\alpha}^{r} - R_s i_{s\alpha}^{r} + \omega_r \psi_{s\beta}^{r}) \\ u_{r\beta}^{r*} = \sigma L_r u_{r\beta}^{'} + R_r i_{r\beta}^{r} + \dfrac{L_m}{L_s} \\ \qquad (u_{s\beta}^{r} - R_s i_{s\beta}^{r} + \omega_r \psi_{s\alpha}^{r}) \end{cases} \tag{17}$$

$$\begin{cases} u_{r\alpha}^{'} = [H_m + H_{a1} + H_{a2}](i_{r\alpha}^{r*} - i_{r\alpha}^{r}) \\ u_{r\beta}^{'} = [H_m + H_{a1} + H_{a2}](i_{r\beta}^{r*} - i_{r\beta}^{r}) \end{cases} \tag{18}$$

where $u_{r\alpha}^{r*}$ and $u_{r\beta}^{r*}$ are reference value of rotor voltage, $i_{r\alpha}^{r*}$ and $i_{r\beta}^{r*}$ are reference value of rotor current.

Figure 5 shows the rotor current control diagram based on the developed PR controller.

Figure 5. Rotor current control scheme based on PR controller.

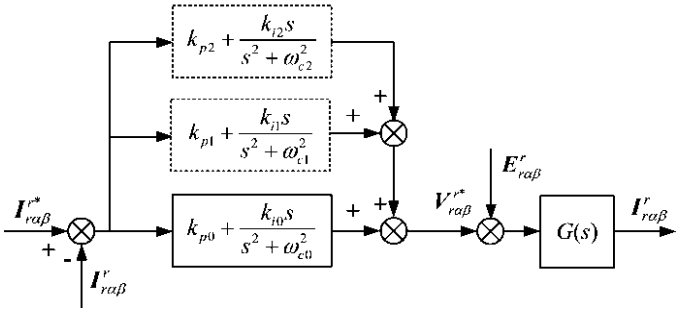

Suppose:

$$\begin{cases} a_1 = (s^2 + \omega_{c0}^2)(s^2 + \omega_{c1}^2)(s^2 + \omega_{c2}^2) \\ a_2 = (s^2 + \omega_{c1}^2)(s^2 + \omega_{c2}^2) \\ a_3 = (s^2 + \omega_{c0}^2)(s^2 + \omega_{c2}^2) \\ a_4 = (s^2 + \omega_{c0}^2)(s^2 + \omega_{c1}^2) \end{cases} \tag{19}$$

where $\omega_{c0} = \omega_s - \omega_r$, $\omega_{c1} = \omega_r$, and $\omega_{c2} = \omega_s + \omega_r$

The closed-loop transfer function of rotor current controller is:

$$F_i(s) = \frac{\boldsymbol{I}_{r\alpha\beta}^{r}(s)}{\boldsymbol{I}_{r\alpha\beta}^{r*}(s)} = \frac{C(s)G(s)}{1 + C(s)G(s)} = \frac{a_1(k_{p0} + k_{p1} + k_{p2}) + a_2 k_{i0} s + a_3 k_{i1} s + a_4 k_{i2} s}{\dfrac{(s^2 + \omega_{c0}^2)(s^2 + \omega_{c1}^2)(s^2 + \omega_{c2}^2)}{G(s)} + M(s)} \tag{20}$$

where:

$$M(s) = a_1(k_{p0} + k_{p1} + k_{p2}) + a_2 k_{i0} s + a_3 k_{i1} s + a_4 k_{i2} s \tag{21}$$

Substituting $s = j(\omega_s - \omega_r)$, $s = -j\omega_r$ and s = $-j(\omega_s + \omega_r)$ into Equation (20) yields:

$$F_i(s) = \frac{\boldsymbol{I}^r_{r\alpha\beta}(s)}{\boldsymbol{I}^{r*}_{r\alpha\beta}(s)} = \frac{M(s)}{M(s)} = 1 \tag{22}$$

It can be implied from Equation (22) that the proposed PR current control scheme can provide zero steady-state error for ac signal with the frequencies of $\omega_s - \omega_r$, ω_r and $\omega_s + \omega_r$ regardless of the parameters L_r, σ, and R_r of DFIG.

From Figure 5, the transfer function between disturbance voltage and given current is calculated as:

$$F_u(s) = \frac{\boldsymbol{I}^r_{r\alpha\beta}(s)}{\boldsymbol{E}^r_{r\alpha\beta}(s)} = \frac{G(s)}{1 - C(s)G(s)} = \frac{(s^2 + \omega_{c0}^2)(s^2 + \omega_{c1}^2)(s^2 + \omega_{c2}^2)}{\dfrac{(s^2 + \omega_{c0}^2)(s^2 + \omega_{c1}^2)(s^2 + \omega_{c2}^2)}{G(s)} + M(s)} \tag{22}$$

Substituting $s = j(\omega_s - \omega_r)$, $s = -j\omega_r$ and $s = -j(\omega_s + \omega_r)$ into (23) results in:

$$F_u(s) = \frac{\boldsymbol{I}^r_{r\alpha\beta}(s)}{\boldsymbol{E}^r_{r\alpha\beta}(s)} = \frac{0}{\dfrac{0}{G(s)} + M(s)} = 0 \tag{23}$$

It is indicated from Equation (24) that the proposed PR control scheme eliminates the corresponding disturbance of respective frequency, regardless of the parameters L_r, σ, and R_r of DFIG.

The PR controller given above can be replaced by a non-ideal PR controller to solve the instability associated with infinite gain at the center frequency of the resonant term. Consequently, the non-ideal PR controller in the control system is given as follows:

$$G_{PR}(s) = k_p + \frac{k_i \omega_i s}{s^2 + 2\omega_i s + \omega_c^2} \tag{24}$$

The bandwidth of the controller is regulated by ω_i in Equation (25), which is helpful in reducing sensitivity to slight frequency variation in a typical grid. It is assumed that the synchronous rotation angular speed ω_s = 120π rad/s and rotor speed ω_r = 100π rad/s, then the resonant angular speed of the main controller is calculated as:

$$\omega_{c0} = \omega_s - \omega_r = 20\pi \ rad/s \tag{25}$$

The resonant angular speeds of the two auxiliary controllers are expressed as:

$$\begin{cases} \omega_{c1} = \omega_r = 100\pi \ rad/s \\ \omega_{c2} = \omega_s + \omega_r = 220\pi \ rad/s \end{cases} \tag{26}$$

The frequency response of resonant controller under different ω_i is depicted in Figure 6. It can be obtained from Figure 6 that the resonant peaks occur only at the selected frequencies of 10, 50, and 110 Hz which are the resonant frequencies of the controller. The controller becomes more selective with a smaller ω_i. However, a smaller ω_i will cause the controller to be more sensitive to frequency variations, which is unfavorable to system stability.

Figure 6. Open loop Bode plot of resonant controller.

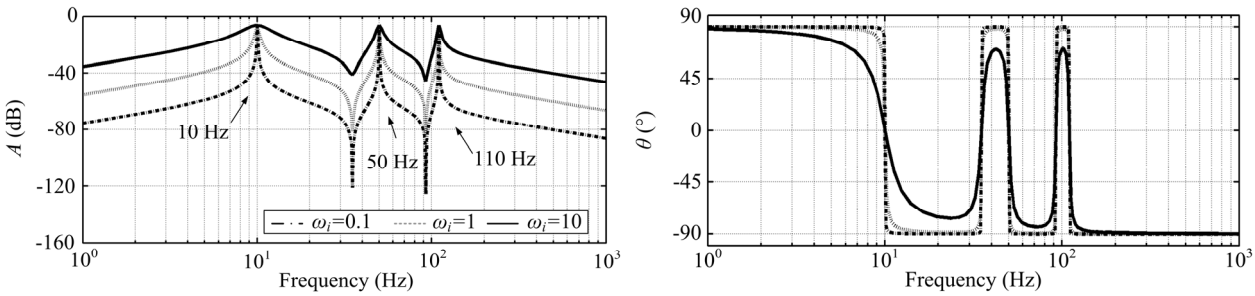

According to Equation (14), a schematic diagram of the PR current control scheme for the rotor side converter of a DFIG is illustrated in Figure 7. Figure 7(a) shows the control structure of the overall system, and Figure 8(b) depicts the proposed current controller. As shown in Figure 7(a), a voltage dips detector (VDD) detects the grid voltage and determines whether or not to switch on the auxiliary controllers. The control system operates in the traditional mode with the auxiliary controllers disabled under normal conditions. When grid voltage dips are detected, the auxiliary controllers will be immediately enabled, generating the corresponding compensation of rotor voltage. As shown in Figure 7(b), the deviation of current is passed to the main controller and auxiliary controllers to generate the required rotor control voltage. The output voltage of the main controller and auxiliary controllers may exceed the capability of the RSC due to the limited voltage rating of the RSC. In order to ensure the normal operation of the DFIG, a rotor voltage limit (RVL) is applied to limit the output of the controller. Space vector modulation is then used to generate the required switching voltage vectors for the RSC to control the DFIG.

Figure 7. Schematic diagram of the proposed control system. (**a**) System control structure; (**b**) Proposed PR current controller.

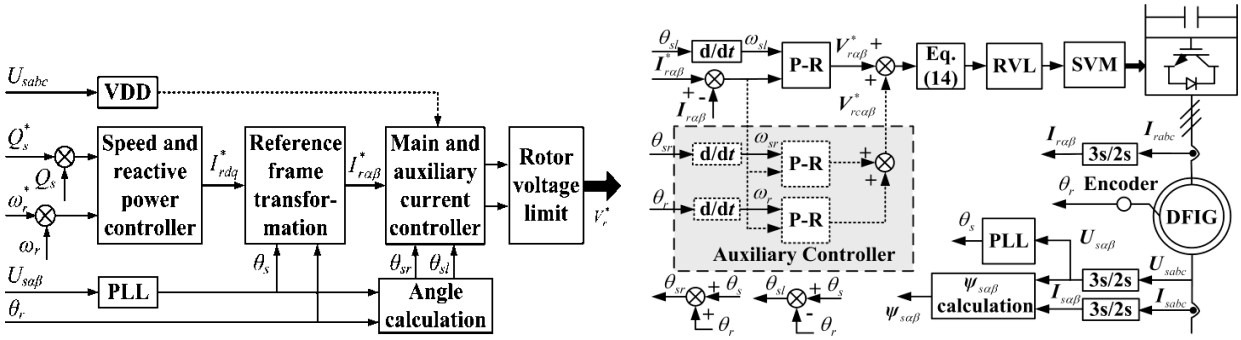

(**a**) (**b**)

At the instant of voltage dips, the output voltage of controller is required to be regulated quickly to suppress the current. The proposed control system will be implemented without the need to decompose the sequential components to improve the response of system. As shown in Figure 8(a), when there is a sudden voltage drop at 0.004 s, the proposed current controller generates the rotor control voltage rapidly and the dynamic process is very short with the maximum rotor voltage being less than 300 V. In [21], the DC component of flux during voltage drop is extracted by a band-pass filter, the current reference value is computed, and then the rotor voltage reference value is generated by the PI

controller. The controller output voltage during voltage drop is shown in Figure 8(b). As can be seen from the figure, the delay of the filter affects the controller response. Compared to Figure 8 (a), a greater rotor voltage is required.

Figure 8. Controller output voltage during voltage drop. (**a**) Proposed PR current controller; (**b**) Current controller in [21].

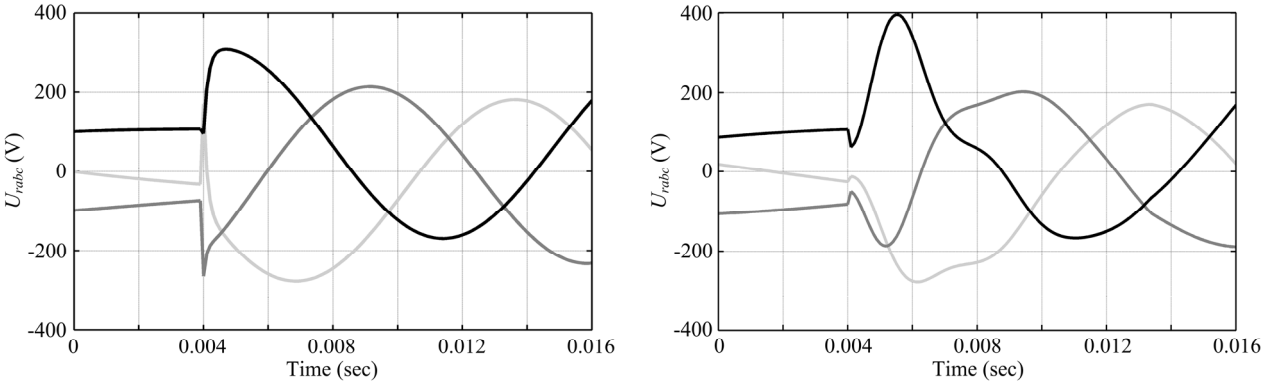

3.2. Simplification of the Auxiliary Controller

The components of the stator flux linkage generated in a grid fault are converted from the static coordinate frame to a negative reference frame rotating at the speed of $-\omega_s/2$:

$$\begin{cases} \boldsymbol{\psi}_{s\alpha\beta+}^{-\frac{1}{2}\omega_s} = \boldsymbol{\psi}_{s\alpha\beta+} e^{j(\frac{3}{2}\omega_s)t} \\ \boldsymbol{\psi}_{s\alpha\beta DC}^{-\frac{1}{2}\omega_s} = \boldsymbol{\psi}_{s\alpha\beta DC} e^{j(\frac{1}{2}\omega_s)t - t/\tau_s} \\ \boldsymbol{\psi}_{s\alpha\beta-}^{-\frac{1}{2}\omega_s} = \boldsymbol{\psi}_{s\alpha\beta-} e^{-j(\frac{1}{2}\omega_s)t} \end{cases} \tag{27}$$

It can be derived from Equation (28) that the components of the stator flux linkage are components with the angular frequencies of $3\omega_s/2$ and $\pm\omega_s/2$. According to Section 2, under grid fault conditions, the rotor current in the negative reference frame rotating at the speed of $-\omega_s/2$ contains ac components with the angular frequencies of both $\pm\omega_s/2$ and $3\omega_s/2$. Since the resonant controller is a doubly-side integrator, the resonant part tuned at the angular frequency of $\omega_s/2$ eliminates the error for both the positive sequence at the frequency of $\omega_s/2$ and the negative sequence at $-\omega_s/2$. Therefore, adoption of the PR controller tuned at $\omega_s/2$ eliminates the errors of the ac signal with the frequencies of $\pm\omega_s/2$.

The auxiliary controllers are simplified as shown in Figure 9. The dc and negative sequence components of current are adjusted only by one PR controller implemented in the reference frame rotating at the speed of $-\omega_s/2$ and the control system is simplified. In addition transforming dc and negative sequence components into ones with the same frequency will effectively eliminate the impact between the various frequency components. It can also regulate the current according to both dc and negative sequence components.

Figure 9. Simplification of the PR controller.

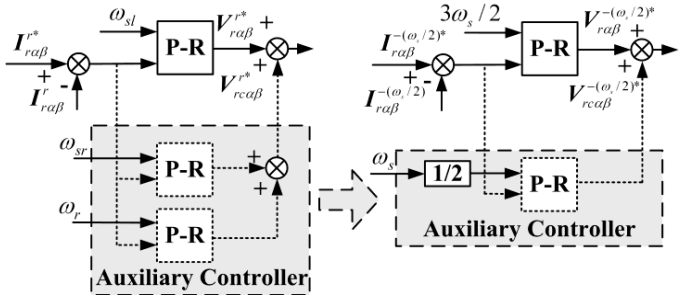

4. Simulation Results

To verify the theory and the proposed PR control strategy, simulation results based on MATLAB/Simulink are provided for a 1.5 MW DFIG-based wind generation system under stator voltage dips caused by grid fault. The system parameters are given in Table 1 [29].

Table 1. DFIG system Parameters.

DFIG Parameters	Value
Rated generator power	1.5 MW
Rated generator voltage	0.575 kV
Frequency	60 Hz
Stator resistance	0.0014 Ω
Stator leakage inductance	8.998×10^{-5} H
Rotor resistance	9.9187×10^{-4} Ω
Rotor leakage inductance	8.2088×10^{-5} H
Magnetizing inductance	1.526×10^{-3} H
Pole pairs	3

The DFIG-based wind generator is controlled by a RSC in the traditional system, and the main objective of the grid-side converter is to control the dc-link voltage by the pulse width modulation method. The dc link voltage is assumed to be 500 V, then the RSC maximum output phase voltage is about 290 V in peak value, and the phase current of rotor is 1.53 kA in RMS and 2.16 kA at peak value. From the analysis in Section 3, it is more difficult for the DFIG to ride through the faults under super-synchronous conditions. Thus, the rotor speed is assumed to be 1500 r/min with the slip $s = -0.25$ in the simulation.

4.1. Three-Phase Fault

Figures 10(a) and (b) compare the simulation results, with the conventional and the proposed control strategies adopted, respectively, when the stator voltage drops to 0.2 pu due to a three-phase fault. The fault occurs at $t = 0.05$ s and is cleared at $t = 0.25$ s.

Figure 10. Simulation results on a DFIG when an 80% balance voltage drop occurs. (**a**) Conventional control; (**b**) Proposed control.

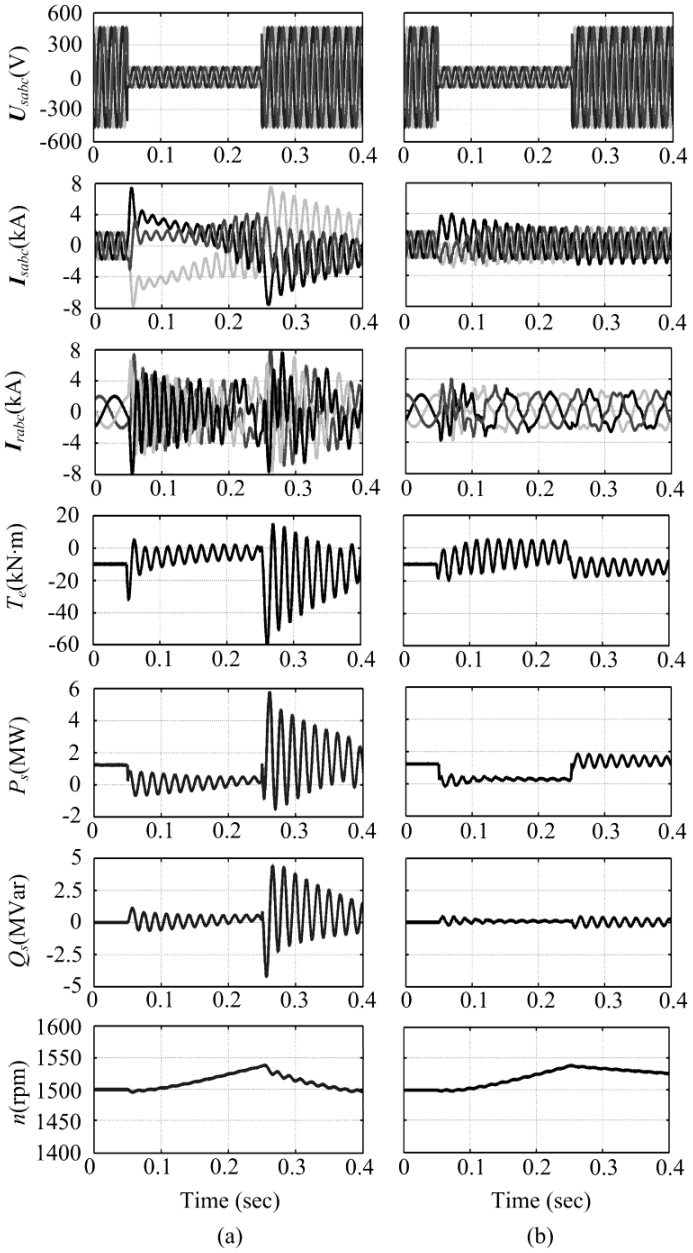

Due to the dc component of the stator flux linkage caused by the stator voltage dips, stator and rotor currents increase dramatically and the rotor current shoots up to 8 kA at the beginning of the voltage dips and the rotor current shoots up and exceeds 8 kA at the moment of grid recovery by the conventional control method. In this process, the rotor current will exceed the maximum value of converter rating and the wind turbine needs to be disconnected from the grid, which is not good for both the normal operation of generator and the grid fault recovery. Stator active/reactive powers and electromagnetic torque result in a great pulsation, hence affecting the stability of the grid and increasing the mechanical stress on the turbine system. Compared with the conventional control strategy, the proposed method is able to suppress the rotor overshoot current to only 4 kA. It is worth noting that there exists some safety margin in power electronic design, so the DFIG can ride through faults using the proposed control scheme. Meanwhile, the pulsations of stator current, stator

active/reactive powers and electromagnetic torque all decrease dramatically, resulting in improved dynamic behaviour of the DFIG under grid fault conditions.

Figure 11. Simulation results on a DFIG when a 50% balance voltage drop occurs. (**a**) Conventional control; (**b**) Proposed control.

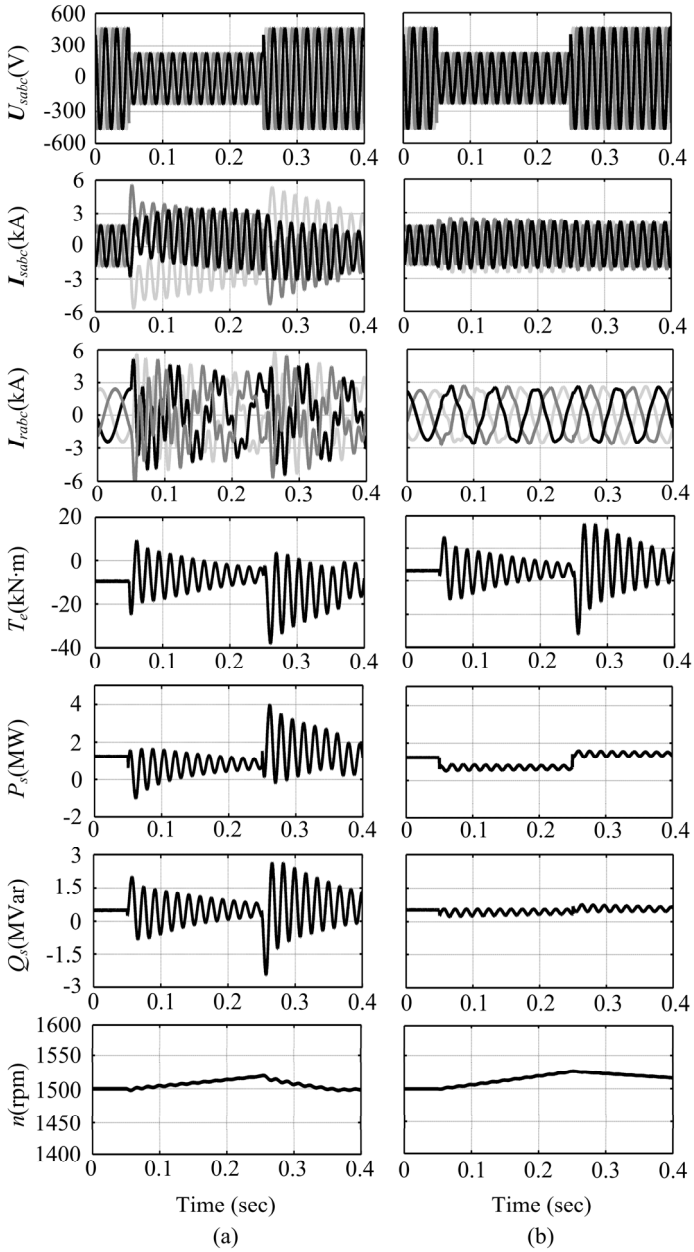

Caused by a three-phase-to-ground fault, the stator voltage drops to 0.5 pu which is simulated with the output reactive power of generator equal to 0.5 MVar. The grid voltage dips at 0.1 s and recovers at 0.5 s in Figure 11. Compared with Figure 10(a), it is shown in Figure 11(a) that the over-current decreases with the adopted traditional control strategy when a fault occurs due to much lower voltage dips. However, a protection system like the crowbar has to be enabled as a result of the over-current. The proposed method is more effective than the traditional method in eliminating rotor fault currents and reducing oscillations of the stator active/reactive power and electromagnetic torque. Also the DFIG provides uninterrupted active/reactive power output to support the grid recovery.

Figure 12. Simulation results on a DFIG when a 70% phase-phase-ground voltage drop occurs. (**a**) Conventional control; (**b**) Proposed control.

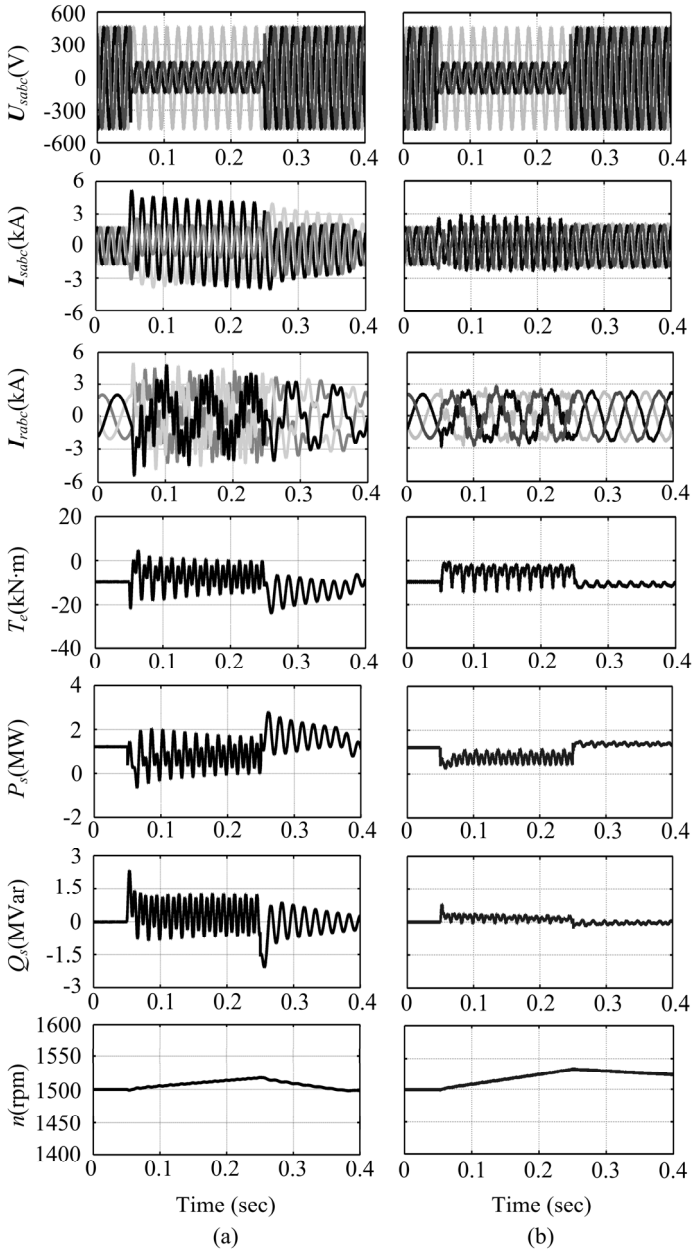

4.2. Phase-Phase-Ground Fault

Figure 12 shows the simulation results with the conventional and the proposed control strategies adopted separately, when the stator voltage drops to 0.3 pu under a phase-phase-ground fault in the grid. The grid voltage dips at 0.05 s and recovers at 0.25 s. Not only does the stator flux have a transitory dc component, such as that originated in symmetrical dips, but it also has a permanent negative sequence component that remains throughout the whole dip, causing a continuous over-current in rotor. As for the traditional control scheme, a continuous over-current appears in both the stator and rotor during the grid fault. Therefore, the protection system should be enabled during the whole process to protect the converter. The wind turbine generator will be disconnected from the grid affecting the grid fault recovery. The proposed control scheme can suppress the rotor fault current

caused by the dc and negative sequence components of the state flux linkage without affecting the performance of the DFIG.

4.3. Control System Analysis

The effect of the controller on a fault current is directly affected by the voltage rating of the RSC. In the normal operation of the DFIG, the RSC output voltage is approximately sV_s [23]. If the magnetizing current is neglected, rotor and stator currents are the same in pu values. DFIG slip is supposed to range from −0.3 to 0.3, which means that the RSC needs to output at least 30% of the stator voltage in pu. Therefore, the rating of the RSC should be 30% of the stator rating at the minimum. In practice, in order to enhance the ability to regulate transient current, RSC ratings will be higher than 30%.

The fault in the paper is supposed to be a three-phase grid fault for the sake of convenience. As a result of stator voltage dips, the dc component φ_{sDC} is generated in the stator flux linkage to maintain conservation which compensates for the flux caused by the dip voltage of V_f. This is equivalent to the static voltage V_f generated in space with the angular speed of ω_r relative to the rotor. Therefore, V_f will have an effect of $(1-s)V_f$ on rotor. To keep the rotor current constant, the supplied rotor voltage of RSC under voltage dips is:

$$\boldsymbol{V}_r = |s|\boldsymbol{V}_s + (1-s)\boldsymbol{V}_f \tag{28}$$

Assuming that the stator voltage is 1 pu, Figure 13 shows the compensation voltage required by the RSC under voltage dips of different levels. As shown in Figure 13, the required maximum voltage of RSC is 0.3 pu under normal conditions. The deeper the voltage dips, the higher the compensation voltage rating that will be required. Compensation voltage of the RSC reaches 1.34 pu if the dip is 80% V_s.

Figure 13. The required output voltage of the RSC under different voltage drop levels.

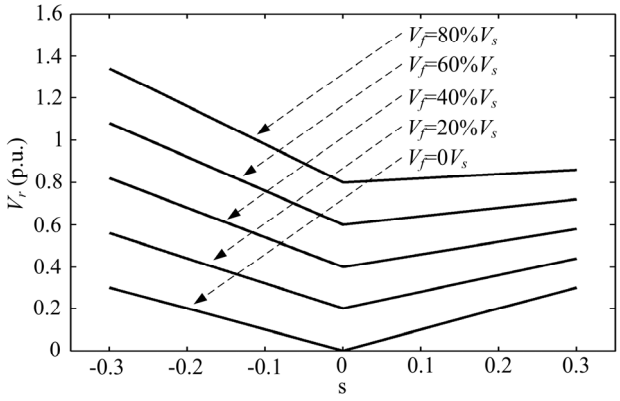

The relationship between the required compensation voltage for RSC and the rotor speed under grid fault is illustrated in Figure 14, which is cut by an auxiliary horizontal plane V_r = 0.6 pu. The faster the rotor speed is, the higher the compensation voltage for RSC required under the same condition is. The compensation voltage reaches the maximum when the DFIG is operated at the maximum super-synchronous speed (s = −0.3). If the stator voltage further drops to 0 V, the required rotor voltage

of RSC needs to be 1.6 pu. In Figure 14, V_r = 0.6 pu represents the maximum output voltage of the RSC under which the RSC is capable of totally eliminating the transient rotor current. Due to the IGBT restrictions, the pulse current rating of the IGBT is typically twice as high as the continuous current rating. Therefore, when the rotor voltage is 0.6 pu, the LVRT of DFIG can operate in a much wider region than that under the surface of V_r = 0.6 pu which means that the LVRT of DFIG can be realized under all conditions, even if the output voltage of the RSC is not at the maximum value of 1.6 pu.

In order to suppress the rotor fault current of the DFIG under grid fault conditions, two main problems need to be solved: accurate detection of the rotor angular frequency and selection of control parameters. The rotor current of tuned frequency can be controlled by setting resonant frequency of the PR controller. Inaccurate detection of grid angular frequency or rotor rotating angular frequency have an impact on the control precision of the PR controller.

Figure 14. Feasible regions depending on the maximum output voltage of the RSC.

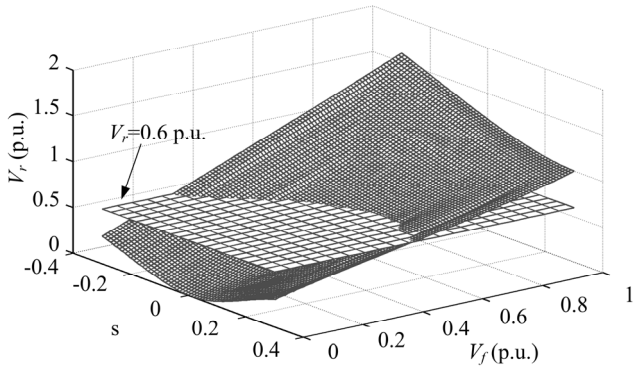

To study the controller performance under a large detection error, simulation analysis of the proposed control scheme is conducted during the three-phase stator voltage drop to 0.2 pu and the two-phase stator voltage drop to 0.2 pu, respectively. Assuming that the actual generator angular frequency is ω_r, the angular frequency is detected to be $\omega_r - 20$.

Figure 15. The effect of detection signal on the peak of rotor current. (**a**) 80% three-phase-to-ground fault; (**b**) 80% phase-phase-to-ground fault.

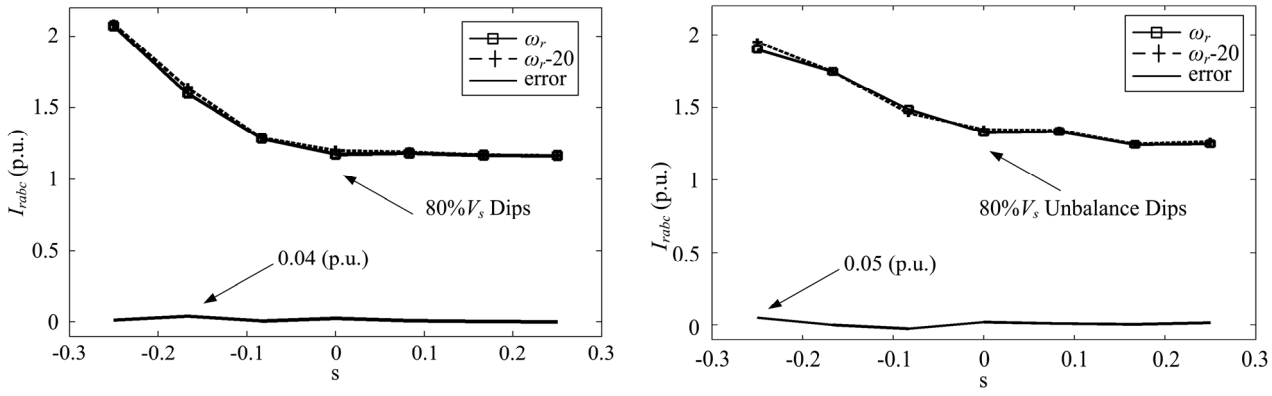

(**a**) (**b**)

Figure 15 shows the effect of detection signal on the peak of rotor current under grid fault conditions. Figure 15(a) shows that the difference of the maximum fault currents before and after the

addition of the detection error is 0.04 pu when the three-phase stator voltage drops to 0.2 pu. Figure 15(b) shows that the difference of the maximum fault currents before and after the addition of detection error is 0.05 pu when the two-phase stator voltage drops to 0.2 pu. It can be drawn from Figures 15(a) and (b) that the controller can suppress rotor fault currents under both symmetric and asymmetric grid fault conditions when the detected angular frequency is inaccurate.

The auxiliary controller should suppress rotor over-currents when grid faults occur. The parameters of the auxiliary controller affect the regulated performance of the rotor current. Bode plot of controller is shown in Figure 16. It can be seen that the bigger the k_p is, the bigger controller gain on other bands, leading to the interference between different frequencies which will further affect the system stability when the amplification gain is up to a certain extent. Therefore, to ensure system stability and good control performance, the k_p value should not be too large.

Figure 16. Bode diagram of PR controller with variation of k_p.

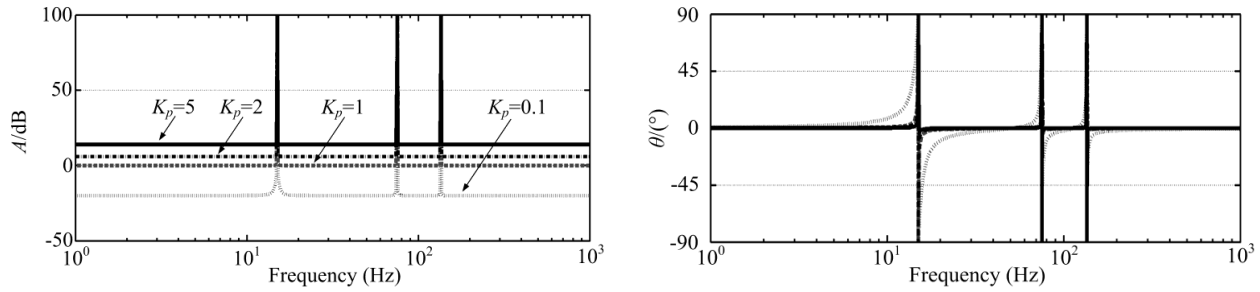

(**a**) (**b**)

The simulation results on the DFIG system with different values of k_p under the 50%, 60%, and 70% of three-phase stator voltage dips, respectively, are shown in Figure 17(a). As shown, when k_p is less than 0.5, the rotor over-current is markedly inhibited by the increase of the k_p value.

Figure 17. The effect of k_p on the peak of rotor current. (**a**) three-phase-to-ground fault; (**b**) phase-phase-to-ground fault.

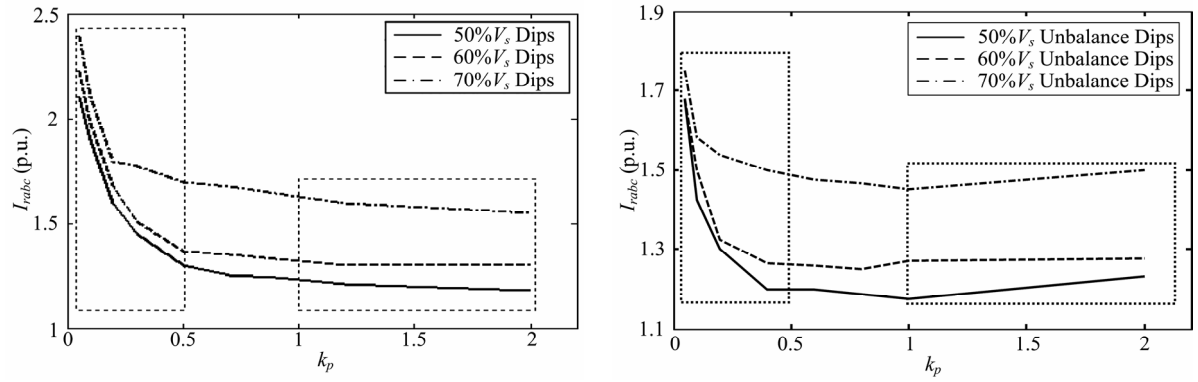

(**a**) (**b**)

However, when k_p is more than 1.0, the rotor over-current does not change significantly with the increase of the k_p value. Figure 17(b) shows the effect of k_p on the peak of rotor current under two-phase stator voltage dip conditions. When k_p is less than 0.5, the rotor over-current is significantly inhibited with the increase of the k_p value. However, when k_p is more than 1.0, the rotor over-current

peak slightly increases under 50% and 70% two-phase stator voltage dips with the increase of the k_p value. This is because when the k_p value reaches a certain extent, controller will produce a gain on other frequencies, which will cause the mutual influence of current with different frequencies, directly affecting over-current suppression.

5. Conclusions

This paper presents a proportional resonance control scheme for a DFIG-based wind power generation system under great-level grid fault conditions. The control system consisting of auxiliary controllers suppresses rotor fault currents effectively, requiring no decomposition or extraction of dc and negative sequence components of the rotor current which improves the response speed of the controller. Therefore, the proposed scheme reduces the occurrence of crowbar interruptions and enhances the operational capability of the DFIG wind turbine. The relationships between the RSC voltage ratings, the rotor speed, and the LVRT capability of the DFIG system are analyzed. With limited RSC voltage ratings, the rotor fault currents of specified frequencies are eliminated to a great extent. The controller performs well, even when the angular frequency detection is not accurate. Simulations have been presented under symmetric and asymmetric grid fault conditions to confirm the analysis and verify the proposed control method. It can be drawn from the simulations that by using the proposed PR scheme the DFIG experiences less rotor fault current and remains in service to continuously supply active/reactive power to grid under grid fault conditions.

Acknowledgments

The authors are grateful to the National Key Basic Research Program of China (973 Program) under Grant 2013CB035602, the Key Program of National Natural Science Foundation of China (51037004), and National Natural Science Foundation of China (51107084) for supporting this work.

References

1. Yamamoto, M.; Motoyoshi, O. Active and reactive power control for doubly-fed wound rotor induction generator. *IEEE Trans. Power Electron*. **1991**, *6*, 624–629.
2. Xia, C.L.; Song, Z.F. Wind energy in China: current scenario and future perspectives. *Renew. Sustain. Energy Rev.* **2009**, *13*, 1966–1974.
3. Pak, L.F.; Dinavahi, V. Real-time simulation of a wind energy system based on the doubly-fed induction generator. *IEEE Trans. Power Syst*. **2009**, *24*, 1301–1309.
4. Slootweg, J.G.; de Haan, S.W.H.; Polinder, H.; Kling, W.L. General model for representing variable speed wind turbines in power system dynamics simulations. *IEEE Trans. Power Syst*. **2003**, *18*, 144–151.
5. Akagi, H.; Sato, H. Control and performance of a doubly-fed induction machine intended for a flywheel energy storage system. *IEEE Trans. Power Electron*. **2002**, *17*, 109–116.
6. Xu, L.; Yao, L.; Sasse, C. Grid integration of large DFIG-based wind farms using VSC transmission. *IEEE Trans. Power Syst.* **2007**, *22*, 976–984.

7. Hughes, F.M.; Anaya-Lara, O.; Jenkins, N.; Strbac, G. Control of DFIG-based wind generation for power network support. *IEEE Trans. Power Syst*. **2005**, *20*, 1958–1966.
8. Xia, C.L.; Gu, X.; Shi, T.N.; Yan, Y. Neutral-Point potential balancing of three-level inverters in direct-driven wind energy conversion system. *IEEE Trans. Energy Convers*. **2011**, *26*, 18-29.
9. Mullane, A.; Lightbody, G.; Yacamini, R. Wind-turbine fault ridethrough enhancement. *IEEE Trans. Power Syst.* **2005**, *20*, 1929–1937.
10. Ng, C.; Ran, L.; Bumby, J. Unbalanced-grid-fault ride-through control for a wind turbine inverter. *IEEE Ind. Appl.* **2008**, *44*, 845–856.
11. Zhou, Y.; Bauer, P.; Ferreira, J.A.; Pierik, J. Operation of grid-connected DFIG under unbalanced grid voltage condition. *IEEE Trans. Energy Convers*. **2009**, *24*, 240–246.
12. Song, Z.F.; Xia, C.L.; Shi, T.N. Assessing transient response of DFIG based wind turbines during voltage dips regarding main flux saturation and rotor deep-bar effect. *Appl. Energy* **2010**, *87*, 3283–3293.
13. Causebrook, A.; Atkinson, D.J.; Jack, A.G. Fault ride-through of large wind farms using series dynamic braking resistors. *IEEE Trans. Power Syst*. **2007**, *22*, 966–975.
14. Morren, J.; de Haan, S.W.H. Ride-through of wind turbines with doubly-fed induction generator during a voltage dip. *IEEE Trans. Energy Convers*. **2005**, *20*, 435–441.
15. Petersson, A.; Harnefors, L.; Thiringer, T. Evaluation of current control methods for wind turbines using doubly-fed induction machines. *IEEE Trans. Power Electron*. **2005**, *20*, 227–235.
16. Morren, J.; de Haan, S.W.H. Short-circuit current of wind turbines with doubly fed induction generator. *IEEE Trans. Energy Convers*. **2007**, *22*, 174–180.
17. Brekken, T.A.; Mohan, N. Control of a doubly fed induction wind generator under unbalanced grid voltage conditions. *IEEE Trans. Energy Convers*. **2007**, *22*, 129–135.
18. Xu, L.; Wang, Y. Dynamic modeling and control of DFIG based wind turbines under unbalanced network conditions. *IEEE Trans. Power Syst*. **2007**, *22*, 314–323.
19. Xu, L. Enhanced control and operation of DFIG-based wind farms during network unbalance. *IEEE Trans. Energy Convers*. **2008**, *23*, 1073–1081.
20. Hu, J.B.; Xu, L. Improved control of DFIG systems during network unbalance using PI–R current regulators. *IEEE Trans. Ind. Electron*. **2009**, *56*, 439–451.
21. Xiang, D.; Ran, L.; Tavner, P.J.; Yang, S. Control of a doubly fed induction generator in a wind turbine during grid fault ride-through. *IEEE Trans. Energy Convers*. **2006**, *21*, 652–662.
22. Hu, J.B.; He, Y.K.; Xu, L. Improved rotor current control of wind turbine driven doubly-fed induction generators during network voltage unbalance. *Electr. Power Syst. Res.* **2010**, *80*, 847–856.
23. Liang, J.; Qiao, W.; Harley, R.G. Feed-forward transient current control for low-voltage ride-through enhancement of DFIG wind turbines. *IEEE Trans. Energy Convers*. **2010**, *25*, 836–843.
24. Teodorescu, R.; Blaabjerg, F.; Liserre, M.; Loh, P.C. Proportional–resonant controllers and filters for grid-connected voltage-source converters. *IEEE Proc. Electr. Power Appl*. **2006**, *153*, 750–762.
25. Zmood, D.N.; Holmes, D.G. Stationary frame current regulation of PWM inverters with zero steady-state error. *IEEE Trans. Power Electron*. **2003**, *18*, 814–822.
26. Chen, W.; Chen, C.; Song, Z.F. Proportional-resonant control for dual PWM converter in doubly fed wind generation system. *Proc. CSEE* **2009**, *29*, 1–7.

27. Timbus, A.; Liserre, M.; Teodorescu, R.; Rodriguez, P.; Blaabjerg, F. Evaluation of current controllers for distributed power generation systems. *IEEE Trans. Power Electron*. **2009**, *24*, 654–664.
28. Liu, C.J.; Blaabjerg, F.; Chen, W.J.; Xu, D.H. Stator current harmonic control with resonant controller for doubly fed induction generator. *IEEE Trans. Power Electron.* **2012**, *27*, 3207–3220.
29. Fadaeinedjad, R.; Moallem, M.; Moschopoulos, G. Simulation of a wind turbine with doubly fed induction generator by FAST and Simulink. *IEEE Trans. Energy Convers*. **2008**, *23*, 690–700.

© 2012 by the authors; licensee MDPI, Basel, Switzerland. This article is an open access article distributed under the terms and conditions of the Creative Commons Attribution license (http://creativecommons.org/licenses/by/3.0/).